

# Calibrated Quantification of the Dark-Exciton Reservoir via a $k$ -Space-Folding Probe

Guangyu Dai,<sup>1</sup> Xinyu Zhang,<sup>1</sup> Zhaoqi Gu,<sup>1</sup> Junyuan Zhang,<sup>1</sup> Lin Dou,<sup>1</sup> Jiaxin Yu,<sup>1,\*</sup> and Fuxing Gu<sup>1</sup>

<sup>1</sup> Laboratory of Integrated Opto-Mechanics and Electronics, School of Optical-Electrical and Computer Engineering, University of Shanghai for Science and Technology, Shanghai 200093, China

Spin-forbidden dark excitons in monolayer transition metal dichalcogenides constitute a dominant ‘hidden reservoir’ that governs exciton dynamics and many-body interactions. Yet determining the population distribution within this reservoir remains challenging because detected brightness conflates radiative-rate modification with collection efficiency, obscuring the link between intensity and population. Here we make this inverse problem well posed by calibrating the position- and orientation-resolved detection response. Combining microsphere-enabled ‘ $k$ -space folding’ with Green-tensor quasinormal-mode calibration, we decouple radiative-rate modification from collection efficiency. We extract a room-temperature dark-to-bright population ratio  $N_D/N_B = 4.3 \pm 1.1$ , consistent with a near-thermalized manifold under continuous-wave excitation. This calibrated population metric provides a quantitative thermodynamic benchmark for the dark reservoir and interaction-driven 2D exciton phases.

Long-lived spin-forbidden dark excitons in monolayer transition-metal dichalcogenides, such as WSe<sub>2</sub>, shape valley/spin relaxation and define the relevant low-energy manifold for interaction-driven exciton phases [1–3]. Yet direct optical readout remains intrinsically difficult due to their slow recombination and, critically, their radiative pattern [4]: while bright excitons radiate into propagating modes with small in-plane wave vector ( $k_{\parallel}$ ), dark excitons predominantly couple to high- $k_{\parallel}$  mode [Fig. 1(a)], largely outside the objective collection cone with finite numerical aperture (NA), making standard far-field collection inefficient. Existing approaches to access dark excitons typically rely on bright–dark mixing [5–7], platform-defined out-coupling [8,9] or antenna effects [10,11]. However, detected intensity entangles population with electromagnetic weighting (radiative-rate modification and collection efficiency), rendering any inversion to reservoir population ill-posed; a calibrated far-field mapping is therefore essential for thermodynamic or many-body inference of the dark reservoir [12,13].

Here, we report the first far-field quantification of dark-exciton populations, in particular the dark-to-bright population ratio in monolayer WSe<sub>2</sub>. We combine a microsphere-enabled ‘ $k$ -space folding’ probe—redirecting high- $k_{\parallel}$  emission into propagating modes within the collection cone [Fig. 1(b)]—with a Green-tensor quasinormal-mode (QNM) calibration that separates out-of-plane and in-plane dipole responses and decouples radiative-rate effects from collection efficiency. Beyond enabling far-field access, our approach provides a route to infer the dark-to-bright population ratio, establishing a thermodynamic anchor for the dark-exciton reservoir under ambient conditions.

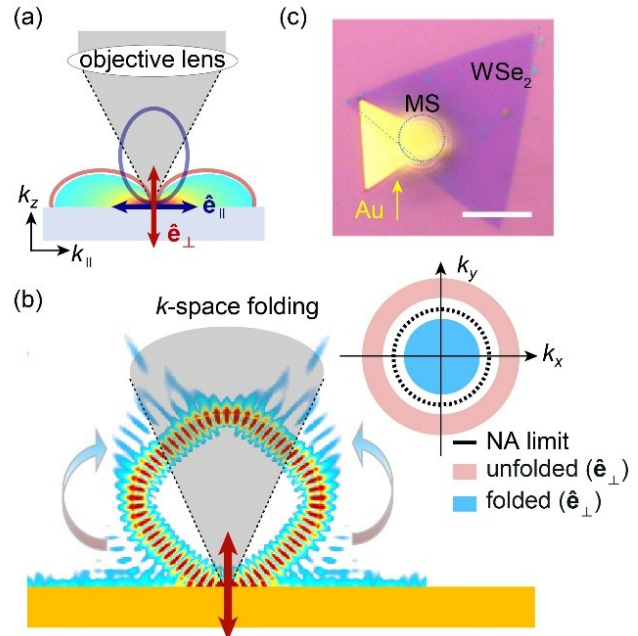


FIG. 1. (a)  $k$ -space radiation contrast for bright and dark excitons. Bright excitons (navy  $\hat{e}_{\parallel}$ ; hollow radiation lobe) emit mainly at low  $k_{\parallel}$  within the NA-limited collection cone (gray), whereas spin-forbidden dark excitons (red  $\hat{e}_{\perp}$ ; colored radiation lobes) carry strong weight at large  $k_{\parallel}$ , mostly outside the collection cone. (b) Microsphere-enabled  $k$ -space folding that redirects dark-exciton high- $k_{\parallel}$  emission into propagating angles within the collection cone. Inset: a  $k$ -space schematic showing that the high- $k_{\parallel}$  emission (pink) is folded into the low- $k_{\parallel}$  region (blue) inside the NA boundary (dashed circle). (c) Optical micrograph of a representative device consisting of a SiO<sub>2</sub> microsphere (MS) on a WSe<sub>2</sub>/Au. Scale bar, 10  $\mu\text{m}$ .

\*Contact author: yujiaxin@usst.edu.cn

The sample is a van der Waals stack consisting of monolayer WSe<sub>2</sub> on single-crystal Au substrate (WSe<sub>2</sub>/Au), with a SiO<sub>2</sub> microsphere placed on top as a probe [Fig. 1(c)]. A continuous-wave (CW) laser is focused through a 100 $\times$  objective (NA = 0.8) for nonresonant excitation. The photoluminescence (PL) collected by the same objective defines the detected signal  $I_{\text{det}}$ . We model  $I_{\text{det}}$  as a population-weighted sum of detected-response functions, i.e.,  $I_{\text{det}} \propto \sum N_i R_i$ ,  $i \in \{\parallel, \perp\}$ , where  $N_i$  is the population in channel  $i$  and  $R_i$  is the corresponding detected response. Here, the out-of-plane ( $\perp$ ) and in-plane ( $\parallel$ ) dipole channels are dominated by dark (D) and bright (B) excitons, respectively [3,4], so  $N_{\perp}/N_{\parallel}$  serves as a proxy for  $N_{\text{D}}/N_{\text{B}}$  (validated below). Detected response  $R_i = \eta_i \Gamma_i$  encapsulates collection efficiency  $\eta_i$  and the environment-modified radiative rate  $\Gamma_i$ , both calibrated within a Green-tensor QNM framework. Therefore, identifiability arises from the distinct position dependences of the calibrated  $R_{\perp}$  and  $R_{\parallel}$  under a spatial scan, enabling an inversion for  $N_{\perp}/N_{\parallel}$ .

The intrinsic radiative-decay rate of dark excitons is much weaker than that of bright excitons. Coupling to surface plasmon polaritons (SPPs) can partially compensate the radiation penalty [14], but does not resolve the bottleneck of inefficient far-field collection. Full-wave simulations in Fig. 2(a) show that with moderate Purcell effect on Au substrates, the signal collected in a finite NA is still dominated by in-plane dipole transition (i.e., out-of-plane  $\eta_{\perp} = 8.7\%$  compared with in-plane  $\eta_{\parallel} = 46.9\%$ ). It is validated by the measured back-focal-plane (BFP) PL pattern from planar WSe<sub>2</sub>/Au [Fig. 2(c), shaded; Fig. 2(d)] [15,28]. With the microsphere probe in place, high- $k_{\parallel}$  evanescent emission (including SPP-mediated components) is outcoupled into propagating angles by breaking in-plane translational symmetry. The resulting  $k$ -space folding transfers the dark-exciton weight into the collection cone [Fig. 1(b)], enabling efficient collection of the dark channels.

To quantify the reshaping of both  $\eta_i$  and  $\Gamma_i$ , we use a Green-tensor QNM calibration [16,17,28]. In each selected spectral window, the optical response is dominated by two degenerate TM-like QNMs, denoted QNM<sub>1</sub> and QNM<sub>2</sub>, which originate from the hybridization of whispering-gallery modes (WGMs) with SPPs [Fig. 1(b)] [28]. By coupling with these two modes [Fig. 2(b)], the out-of-plane collection efficiency increases from  $\eta_{\perp} = 8.7\%$  to 43.4% ( $\approx 5\times$ ), while the in-plane channel changes only modestly (from  $\eta_{\parallel} = 46.9\%$  to 54.0%). The microsphere, which selectively enhances the out-of-plane response, provides a comparably efficient far-field probe for both exciton channels [Fig. 2(c), blue curve; Fig. 2(e)].

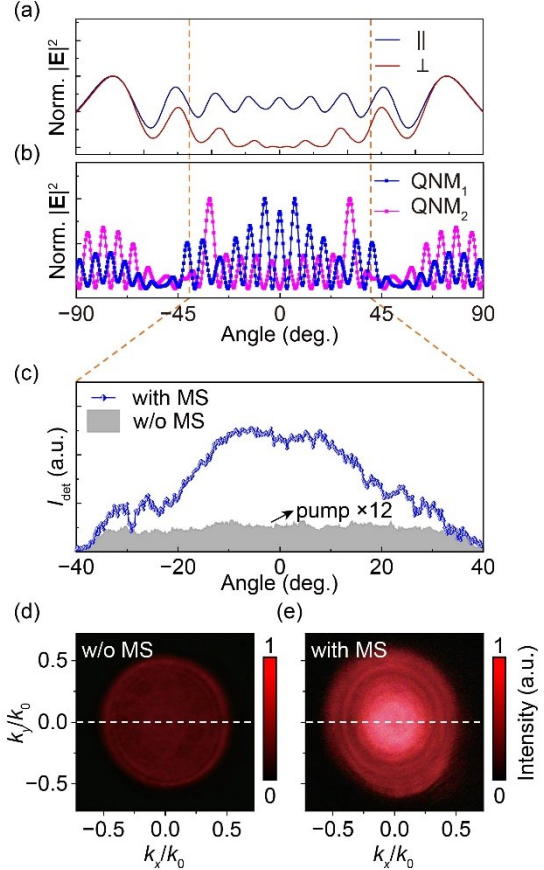


FIG. 2. (a) Simulated angle-resolved emission bright ( $\parallel$ ) and dark ( $\perp$ ) excitons on Au substrates. The dashed line marks the objective collection boundary. (b) Simulated angle-resolved emission of QNM<sub>1,2</sub>. (c) Measured angle-resolved distributions extracted from BFP PL images of WSe<sub>2</sub>/Au recorded with (blue) and without (shaded) the microsphere probe. (d,e) Representative BFP images without and with the probe, respectively. Axes are in units of  $k_0 = \omega/c$ , with  $k_x$  and  $k_y$  the in-plane wave-vector components. Pump power for (d) is 12 $\times$  that for (e).

The system modification to radiative rate  $\Gamma$  can also be derived from the identical tensor. For a dipole at  $\mathbf{r}_0$  with unit vector  $\hat{\mathbf{e}}_i$ , the orientation-resolved decay enhancement follows the dipole-projected local density of optical states (LDOS):

$$\text{LDOS}_i(\mathbf{r}_0, \omega) = \frac{2\omega}{\pi c^2} \hat{\mathbf{e}}_i \cdot \text{ImG}(\mathbf{r}_0, \mathbf{r}_0; \omega) \cdot \hat{\mathbf{e}}_i, \quad (1)$$

where  $\hat{\mathbf{e}}_{\parallel}(\hat{\mathbf{e}}_{\perp})$  denotes the in-plane (out-of-plane) unit dipoles. Equation (1) directly sets the total decay-rate enhancement (radiative and nonradiative) imposed by the environment [28]. QNM-contributed LDOS maps reveal strong orientation selectivity; we take QNM<sub>1</sub> as an example. Along the material plane [dashed lines in

Figs. 3(a) and 3(b)], the in-plane channel couples weakly to QNM<sub>1</sub> [Fig. 3(c)], whereas the out-of-plane channel remains well aligned with the mode field over  $a \geq 1 \mu\text{m}$  footprint [Fig. 3(d)], producing a  $\sim 40 \times$  larger LDOS than that of in-plane channel. QNM<sub>2</sub> exhibits the same trend [28]. To derive  $R_i$ , the radiative rate  $\Gamma_i \equiv \Gamma_{\text{rad},i}$  is then extracted by using the modification factor  $F_{r,i}$  and the free-space radiative rate for dark (bright) excitons  $\Gamma_{0,\perp(\parallel)}$  via  $\Gamma_i = F_{r,i} \Gamma_{0,i}$ . At the optimal position,  $F_{r,\perp}$  exceeds  $F_{r,\parallel}$  by  $\sim 37 \times$  [Fig. 3(e)], roughly compensating the inefficient radiation of dark excitons (i.e.,  $\Gamma_{0,\perp} \approx 10^{-2} \Gamma_{0,\parallel}$ ), allowing the population quantification.

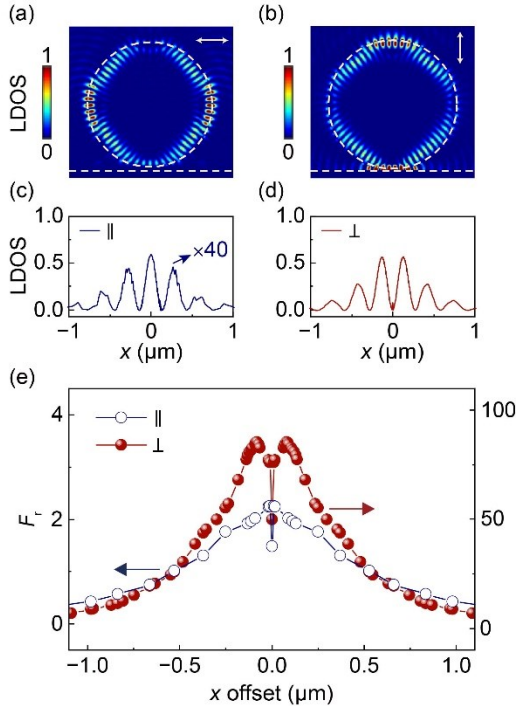


FIG. 3. (a,b) Dipole-projected LDOS contribution of the dominant, degenerate TM-like QNM pair, shown for a representative mode (QNM<sub>1</sub>), for in-plane (a) and out-of-plane dipoles (b) computed over an  $8 \times 8 \mu\text{m}^2$  region. (c,d) LDOS line cuts along the straight dashed lines in (a) and (b). (e) Simulated radiative-rate modification factor  $F_r$  for in-plane ( $\parallel$ , open symbols) and out-of-plane dipoles ( $\perp$ , solid symbols).

The comparable and quantified collection efficiency  $\eta_i$  and radiative-rate  $\Gamma_i$  then provide a route to population retrieval by entering the detected-response functions  $R_i$  [28]. The measured signal can be written as a linear superposition,

$$I_{\text{det}} = a(N_{\parallel}R_{\parallel} + N_{\perp}R_{\perp}), \quad (2)$$

Here  $a$  is a global scaling factor accounting for the total instrumental response. Due to the different

position-dependence of  $R_{\parallel}$  and  $R_{\perp}$ , the population ratio  $N_{\perp}/N_{\parallel}$  can be quantitatively derived from a two-parameter fit to Eq. (2).

The position-dependent detection response is experimentally implemented by translating the excitation spot relative to the microsphere center with a lateral offset  $x$  [Fig. 4(a)]. To accommodate the dark–bright splitting  $\Delta E_{\text{DB}} \equiv E_{\text{B}} - E_{\text{D}} \simeq 40 \text{ meV}$  in monolayer WSe<sub>2</sub> [18], we use  $\sim 6.5\text{-}\mu\text{m}$ -diameter microspheres with a free spectral range of  $\sim 43 \text{ meV}$ , such that the bright and dark emissions at 1.669 eV and 1.625 eV can be aligned with two adjacent resonances [28]. The spectrally integrated detected intensity in the dark window  $I_{\text{det}}^{\text{D}}$  shows an extended plateau followed by a decay across the scan, whereas the intensity in the bright window  $I_{\text{det}}^{\text{B}}$  drops more rapidly with  $x$  [Fig. 4(b)]. The markedly different spatial weights of the two channels make the inversion well-conditioned.

To account for the finite excitation profile  $P(x)$ , we convolve the response function in Eq. (2) as  $\bar{R}_i(x) = \int R_i(u)P_i(u-x)du$  [Fig. 4(c)]. Owing to the microsphere lensing,  $P(x)$  is nearly invariant across the scan (FWHM  $\approx 280 \text{ nm}$ ) [28], so we treat  $N_i$  as position-independent. We then fit the two spectral-window traces separately using  $I_{\text{det}}^{\text{B(D)}}(x) = A^{\text{B(D)}} \bar{R}_{\parallel}(x) + B^{\text{B(D)}} \bar{R}_{\perp}(x)$ . The fits yield  $A^{\text{D}} \simeq 0$  and  $B^{\text{B}} \simeq 0$  within uncertainty [28], indicating that the in-plane (out-of-plane) contribution to the dark (bright) window is negligible, consistent with selective WGM–exciton resonance in the two windows. The uncertainty is dominated by the calibration of  $R_i$  (QNM parameter extraction and spectral-window choice) and by spatial registration in the scan [28]. With the cross terms suppressed,  $A^{\text{B}} \equiv aN_{\parallel}$  and  $B^{\text{D}} \equiv aN_{\perp}$ , and we extract the relative populations as  $N_{\perp}/N_{\parallel} = B^{\text{D}}/A^{\text{B}} = 4.3 \pm 1.1$ .

To verify that the dominant, out-of-plane population originates from the dark-exciton reservoir rather than from disorder-induced out-of-plane projections of bright excitons, we compare the temperature dependence of the QNM-coupled intensity with the direct planar PL of WSe<sub>2</sub>/Au [Fig. 5(a)], the latter being bright-exciton dominated. The two signals show only weak correlation [Pearson coefficient  $r = 0.22$ , Fig. 5(d)] even in the 230–290 K range where thermal redistribution between dark and bright states is expected to be most pronounced. As a material control, we use MoSe<sub>2</sub>/Au [Fig. 5(b)], where  $\Delta E_{\text{DB}} \approx -1.5 \text{ meV}$  places the bright state slightly below the dark state [19,20]; as a structural control, we use WSe<sub>2</sub>/SiO<sub>2</sub> without plasmonic enhancement [Fig. 5(c)] where dark excitons are less radiative. In both control samples, the QNM-coupled emission positively correlates with the planar PL [ $r = 0.77$  and 0.68, respectively, Figs. 5(e) and 5(f)], consistent with a bright-exciton-dominated origin. The contrasted

temperature-dependent correlations between WSe<sub>2</sub>/Au and control groups therefore provide unequivocal evidence that the captured signal is an intrinsic signature of the dark-exciton reservoir rather than a geometric artifact [28].

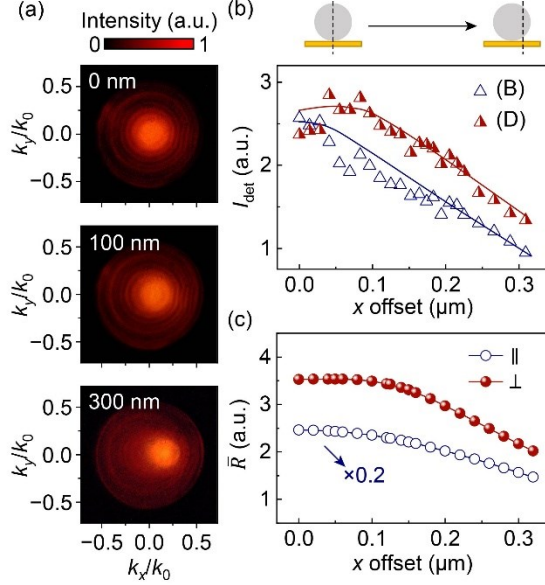


FIG. 4. (a) Representative BFP images recorded (no spectral filtering) at lateral excitation offsets  $x = 0, 100$ , and  $300$  nm relative to the microsphere center. (b) Spectrally integrated detected PL intensity versus  $x$  for the dark window  $I_{\text{det}}^D$  (red symbols) and the bright window  $I_{\text{det}}^B$  (blue symbols). The solid lines are guides to the eye. (c) Excitation convolved, position-dependent response functions  $\bar{R}_{\parallel}$  (open symbols) and  $\bar{R}_{\perp}$  (solid symbols).  $\bar{R}_{\parallel}$  is rescaled for clarity.

In quasi-thermal equilibrium, the dark- and bright-exciton populations (i.e.,  $N_D$  and  $N_B$ ) follow Boltzmann statistics,

$$\frac{N_D}{N_B} = \exp\left(\frac{\Delta E_{\text{DB}}}{k_B T}\right), \quad (3)$$

where  $T$  is the effective exciton temperature. The dark-bright splitting for monolayer WSe<sub>2</sub> predicts  $N_D/N_B \simeq 4.9$  at 300 K. While nonresonant CW driving can, in principle, sustain an exciton temperature different from the lattice temperature, our measured ratio  $N_{\perp}/N_{\parallel} \simeq N_D/N_B$  at  $T \approx 300$  indicates near-thermalization of the exciton manifold in the steady state [21]. We attribute this to the suppressed recombination of bright excitons on Au, and ultrafast phonon-assisted energy relaxation and bright-dark conversion at room temperature [1,22–24]. The redistribution times are predicted to be sub-picosecond to a few picoseconds, two to three orders of magnitude faster than the lifetime of the exciton reservoir [10,25]. Each injected

exciton therefore undergoes many phonon- and spin-flip scattering events before recombination [21,26]. Consequently, the lower-energy dark states accumulate a significant population, acting as a ‘hidden’ thermodynamic sink that obeys lattice-temperature statistics.

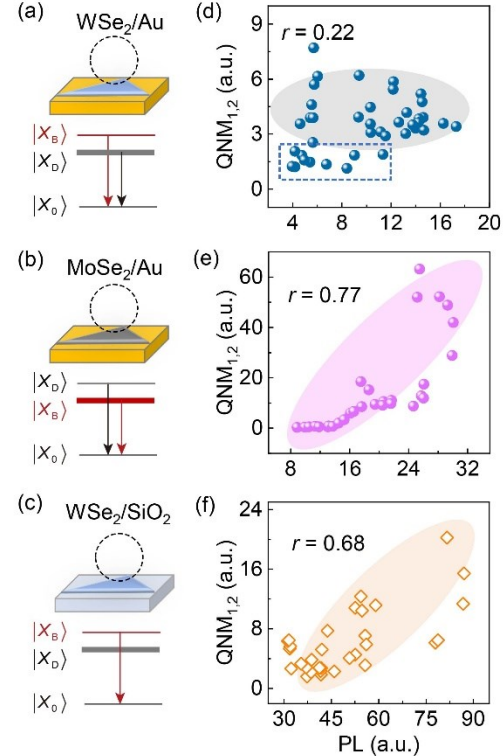


FIG. 5. (a–c) Schematic exciton band structure and optically allowed radiative transitions for WSe<sub>2</sub>/Au (a), MoSe<sub>2</sub>/Au (b), and WSe<sub>2</sub>/SiO<sub>2</sub> (c). Arrows indicate allowed radiative transitions from the bright- ( $|X_B\rangle$ ) or dark-exciton ( $|X_D\rangle$ ) states. (d–f) Correlation between the QNM-mediated emission and the bright-exciton-dominated PL for the same samples in (a–c).  $r$  denotes correlation coefficient. The dashed box in (d) highlights the data acquired in the temperature range 230–295 K.

This calibrated population metrology turns the optically hidden dark reservoir into a thermodynamic observable. In a companion work using the same architecture, we reported phase-resolved, room-temperature Berezinskii–Kosterlitz–Thouless (BKT)-type condensation of dark excitons with algebraic order approaching the universal criterion [27]. Mutually reinforcing thermodynamic and coherence diagnostics establish quasi-thermal equilibrium and a BKT-type hallmark under CW driving, forming a two-pronged benchmark for room-temperature exciton phases. Importantly, the same high-contrast far-field

readout enables scan-based mapping of steady-state dark reservoirs across unpatterned monolayers [28], providing spatial access to disorder, strain, and engineered potentials.

In summary, we establish a calibrated far-field route to retrieve dark-exciton populations in monolayer WSe<sub>2</sub> by combining microsphere-enabled *k*-space folding with a Green-tensor QNM calibration that separates radiative-rate modification from collection efficiency. Unlike approaches that concentrate brightness enhancement, our scheme functions as a calibrated probe linking detected photons to underlying reservoir population under ambient conditions without requiring ultrahigh-Purcell enhancement. The accuracy is ultimately set by the stability of the optical response and the chosen spectral window [28]. Looking forward, the same calibration concept should be extendable to other elusive out-of-plane dipoles, such as hBN defects and interlayer/moiré excitons, enabling quantitative access to hidden reservoirs in broader 2D systems.

This work was supported by National Natural Science Foundation of China (grant Nos. 12074259 and 62122054).

G. D. and X. Z. contributed equally to this work.

- [1] X.X. Zhang, Y. You, S.Y. Zhao, T.F. Heinz, Experimental evidence for dark excitons in monolayer WSe<sub>2</sub>, *Phys. Rev. Lett.* **115**, 257403 (2015).
- [2] E. Liu, J. van Baren, Z. Lu, M.M. Altairy, T. Taniguchi, K. Watanabe, D. Smirnov, C.H. Lui, Gate tunable dark trions in monolayer WSe<sub>2</sub>, *Phys. Rev. Lett.* **123**, 027401 (2019).
- [3] M.R. Molas, A.O. Slobodeniuk, T. Kazimierczuk, K. Nogajewski, M. Bartos, P. Kapuscinski, K. Oreszczuk, K. Watanabe, T. Taniguchi, C. Faugeras, P. Kossacki, D.M. Basko, M. Potemski, Probing and manipulating valley coherence of dark excitons in monolayer WSe<sub>2</sub>, *Phys. Rev. Lett.* **123**, 096803 (2019).
- [4] G. Wang, C. Robert, M.M. Glazov, F. Cadiz, E. Courtade, T. Amand, D. Lagarde, T. Taniguchi, K. Watanabe, B. Urbaszek, X. Marie, In-plane propagation of light in transition metal dichalcogenide monolayers: Optical selection rules, *Phys. Rev. Lett.* **119**, 047401 (2017).
- [5] Z. Li, T. Wang, C. Jin, Z. Lu, Z. Lian, Y. Meng, M. Blei, S. Gao, T. Taniguchi, K. Watanabe, T. Ren, S. Tongay, L. Yang, D. Smirnov, T. Cao, S.F. Shi, Emerging photoluminescence from the dark-exciton phonon replica in monolayer WSe<sub>2</sub>, *Nat. Commun.* **10**, 2469 (2019).
- [6] X.X. Zhang, T. Cao, Z. Lu, Y.C. Lin, F. Zhang, Y. Wang, Z. Li, J.C. Hone, J.A. Robinson, D. Smirnov, S.G. Louie, T.F. Heinz, Magnetic brightening and control of dark excitons in monolayer WSe<sub>2</sub>, *Nat. Nanotechnol.* **12**, 883 (2017).
- [7] R. Ohta, H. Okamoto, T. Tawara, H. Gotoh, H. Yamaguchi, Dynamic control of the coupling between dark and bright excitons with vibrational strain, *Phys. Rev. Lett.* **120**, 267401 (2018).
- [8] X. Ma, K. Kudtarkar, Y. Chen, P. Cunha, Y. Ma, K. Watanabe, T. Taniguchi, X. Qian, M.C. Hipwell, Z.J. Wong, S. Lan, Coherent momentum control of forbidden excitons, *Nat. Commun.* **13**, 6916 (2022).
- [9] J. Wragg, L. Bolzonello, L. Donati, K.P. Soundarapandian, R. Bertini, S.A. Tongay, K. Watanabe, T. Taniguchi, F.H.L. Koppens, N.F. van Hulst, Dual action spectroscopy exposes the bright and dark excitons of room-temperature WSe<sub>2</sub>, *Nano. Lett.* **25**, 7658 (2025).
- [10] S. Jin, F. Liu, I. Razdolski, T.W. Lo, Y. Wang, Z. Peng, K. Liang, Y. Zhu, W. Yao, A.V. Zayats, D. Lei, Plasmonic tuning of dark-exciton radiation dynamics and far-field emission directionality in monolayer WSe<sub>2</sub>, *Sci. Adv.* **12**, eaea5781 (2026).
- [11] K.D. Park, T. Jiang, G. Clark, X. Xu, M.B. Raschke, Radiative control of dark excitons at room temperature by nano-optical antenna-tip Purcell effect, *Nat. Nanotechnol.* **13**, 59 (2018).
- [12] M. Combescot, O. Betbeder-Matibet, R. Combescot, Bose-Einstein condensation in semiconductors: The key role of dark excitons, *Phys. Rev. Lett.* **99**, 176403 (2007).
- [13] J. Bloch, I. Carusotto, M. Wouters, Non-equilibrium Bose-Einstein condensation in photonic systems, *Nat. Rev. Phys.* **4**, 470 (2022).
- [14] Y. Zhou, G. Scuri, D.S. Wild, A.A. High, A. Dibos, L.A. Jauregui, C. Shu, K. De Greve, K. Pistunova, A.Y. Joe, T. Taniguchi, K. Watanabe, P. Kim, M.D. Lukin, H. Park, Probing dark excitons in atomically thin semiconductors via near-field coupling to surface plasmon polaritons, *Nat. Nanotechnol.* **12**, 856 (2017).
- [15] R. Rohrich, C. Hoekmeijer, C.I. Osorio, A.F. Koenderink, Quantifying single plasmonic nanostructure far-fields with interferometric and polarimetric *k*-space microscopy, *Light:Sci. Appl.* **7**, 65 (2018).
- [16] P.T. Kristensen, K. Herrmann, F. Intravaia, K. Busch, Modeling electromagnetic resonators using quasinormal modes, *Adv. Opt. Photonics* **12**, 612 (2020).
- [17] J.J. Ren, S. Franke, B. Vandrunen, S. Hughes, Classical Purcell factors and spontaneous emission decay rates in a linear gain medium, *Phys. Rev. A* **109**, (2024).
- [18] H. Dery, Y. Song, Polarization analysis of excitons in monolayer and bilayer transition-metal dichalcogenides, *Phys. Rev. B* **92**, 125431 (2015).

- [19] C. Robert, B. Han, P. Kapuscinski, A. Delhomme, C. Faugeras, T. Amand, M.R. Molas, M. Bartos, K. Watanabe, T. Taniguchi, B. Urbaszek, M. Potemski, X. Marie, Measurement of the spin-forbidden dark excitons in  $\text{MoS}_2$  and  $\text{MoSe}_2$  monolayers, *Nat. Commun.* **11**, 4037 (2020).
- [20] J.P. Echeverry, B. Urbaszek, T. Amand, X. Marie, I.C. Gerber, Splitting between bright and dark excitons in transition metal dichalcogenide monolayers, *Phys. Rev. B* **93**, 121107 (2016).
- [21] G. Moody, J. Schaibley, X. Xu, Exciton dynamics in monolayer transition metal dichalcogenides, *J Opt Soc Am B* **33**, C39 (2016).
- [22] C. Trovatello, F. Katsch, N.J. Borys, M. Selig, K. Yao, R. Borrego-Varillas, F. Scotognella, I. Kriegel, A. Yan, A. Zettl, P.J. Schuck, A. Knorr, G. Cerullo, S.D. Conte, The ultrafast onset of exciton formation in 2D semiconductors, *Nat. Commun.* **11**, 5277 (2020).
- [23] K. Mourzidis, V. Jindal, M. Glazov, A. Balocchi, C. Robert, D. Lagarde, P. Renucci, L. Lombez, T. Taniguchi, K. Watanabe, T. Amand, S. Francoeur, X. Marie, Exciton formation in two-dimensional semiconductors, *Phys. Rev. X* **15**, 031078 (2025).
- [24] H.-Y. Chen, D. Sangalli, M. Bernardi, First-principles ultrafast exciton dynamics and time-domain spectroscopies: Dark-exciton mediated valley depolarization in monolayer  $\text{WSe}_2$ , *Phys. Rev. Res.* **4**, 043203 (2022).
- [25] C. Robert, T. Amand, F. Cadiz, D. Lagarde, E. Courtade, M. Manca, T. Taniguchi, K. Watanabe, B. Urbaszek, X. Marie, Fine structure and lifetime of dark excitons in transition metal dichalcogenide monolayers, *Phys. Rev. B* **96**, 155423 (2017).
- [26] Y.-h. Chan, J.B. Haber, M.H. Naik, S.G. Louie, J.B. Neaton, F.H. da Jornada, D.Y. Qiu, Exciton thermalization dynamics in monolayer  $\text{MoS}_2$ : A first-principles Boltzmann equation study, *Phys. Rev. B* **111**, 184305 (2025).
- [27] J. Yu, G. Dai, S. Xing, W. Zhang, L. Dou, T. Shen, X. Zhang, X. Feng, and F. Gu, Direct observation of room-temperature exciton condensation, arXiv:2511.09187 (2025).
- [28] See Supplemental Material at [URL] for detailed description of experimental conditions, additional data, and discussions, which includes Refs. [29–33].
- [29] F. Liao, J. Yu, Z. Gu, Z. Yang, T. Hasan, S. Linghu, J. Peng, W. Fang, S. Zhuang, M. Gu, F. Gu, Enhancing monolayer photoluminescence on optical micro/nanofibers for low-threshold lasing, *Sci. Adv.* **5**, eaax7398 (2019).
- [30] J.X. Yu, S. Xing, G.Y. Dai, S.Y. Ling-Hu, F.X. Gu, Direct-bandgap bilayer  $\text{WSe}_2$ /microsphere monolithic cavity for low-threshold lasing, *Adv. Mater.* **34**, e2106502 (2022).
- [31] Y.J. Li, C.Y. Qiu, H.J. Ji, S.Y. Duan, F. Qin, Z.Y. Li, P. Chen, J.W. Huang, G.L. Yu, H.T. Yuan, Microsphere-aided super-resolution scanning spectral and photocurrent microscopy for optoelectronic devices, *Adv. Opt. Mater.* **11**, 2300172 (2023).
- [32] Q. Bai, M. Perrin, C. Sauvan, J.P. Hugonin, P. Lalanne, Efficient and intuitive method for the analysis of light scattering by a resonant nanostructure, *Opt. Express* **21**, 27371 (2013).
- [33] S. Du, F. Jin, X. Liu, X. Huang, Y. Yang, H. Yang, J. Li, Q. Zhang, S. Meng, Y. Guo, C. Gu, Brightening and control of spin - forbidden dark excitons in a strained monolayer semiconductor, *Laser Photonics Rev.* **17**, 2300185 (2023).